

GPS phase scintillation associated with optical auroral emissions: First statistical results from the geographic South Pole

Joe Kinrade,¹ Cathryn N. Mitchell,¹ Nathan D. Smith,¹ Yusuke Ebihara,² Allan T. Weatherwax,³ and Gary S. Bust⁴

Received 11 January 2013; revised 22 February 2013; accepted 7 March 2013; published 15 May 2013.

[1] Ionospheric irregularities affect the propagation of Global Navigation Satellite System (GNSS) signals, causing radio scintillation. Particle precipitation from the magnetosphere into the ionosphere, following solar activity, is an important production mechanism for ionospheric irregularities. Particle precipitation also causes the aurorae. However, the correlation of aurorae and GNSS scintillation events is not well established in literature. This study examines optical auroral events during 2010–2011 and reports spatial and temporal correlations with Global Positioning System (GPS) L1 phase fluctuations using instrumentation located at South Pole Station. An all-sky imager provides a measure of optical emission intensities ([OI] 557.7 nm and 630.0 nm) at auroral latitudes during the winter months. A collocated GPS antenna and scintillation receiver facilitates superimposition of auroral images and GPS signal measurements. Correlation statistics are produced by tracking emission intensities and GPS L1 σ_{ϕ} indices at E and F-region heights. This is the first time that multi-wavelength auroral images have been compared with scintillation measurements in this way. Correlation levels of up to 74% are observed during 2–3 hour periods of discrete arc structuring. Analysis revealed that higher values of emission intensity corresponded with elevated levels of σ_{ϕ} . The study has yielded the first statistical evidence supporting the previously assumed relationship between the aurorae and GPS signal propagation. The probability of scintillation-induced GPS outages is of interest for commercial and safety-critical operations at high latitudes. Results in this paper indicate that image databases of optical auroral emissions could be used to assess the likelihood of multiple satellite scintillation activity.

Citation: Kinrade, J., C. N. Mitchell, N. D. Smith, Y. Ebihara, A. T. Weatherwax, and G. S. Bust (2013), GPS phase scintillation associated with optical auroral emissions: First statistical results from the geographic South Pole, *J. Geophys. Res. Space Physics*, 118, 2490–2502, doi:10.1002/jgra.50214.

1. Introduction

[2] In January 2010, a Novatel GSV4004 Global Positioning System (GPS) scintillation receiver was installed at the South Pole. The receiver can track up to 11 satellites simultaneously, recording high data-rate (50 Hz) measurements of L1 signal amplitude and phase fluctuation [Van Dierendock, 1999]. The antenna is collocated with an all-sky imager (ASI), which provides continuous horizon-to-horizon images of optical

auroral emission intensities within the central Antarctic plateau during the dark winter months. Within the last few decades, technological advances in the fields of optics and image processing have accelerated the study of optical aurora. Satellite-based cameras have profiled the auroral ovals and their large-scale morphology, even on planets other than our own [e.g., Donovan *et al.*, 2006; Hill, 2004; Obara and Fukui, 1997]. Of significance are the recently observed asymmetries in auroral intensities between the northern and southern hemispheres [Laundal and Østgaard, 2009]. Ground-based and multiple-aspect camera studies allow the determination and reconstruction of auroral structuring at continental and meso-scale [Donovan *et al.*, 2006; Frey *et al.*, 1998; Rees *et al.*, 2000] down to much smaller scales, such as curls and boundary undulations (tens of kilometers to hundreds of meters) [Dahlgren *et al.*, 2010; Sandahl *et al.*, 2011]. Davis [1978] provides an accessible guide to auroral structures and their processes; a more recent review of the multiple scales present in auroral plasmas is given by Galperin [2001].

[3] At high latitudes, GPS scintillation is attributed to ionospheric irregularities (on the scale of tens of kilometers down to hundreds of meters at GPS frequencies) and gradients in

¹Department of Electronic and Electrical Engineering, University of Bath, Bath, UK.

²Research Institute for Humanosphere (RISH), Kyoto University, Kyoto, Japan.

³Department of Physics, Siena College, New York, New York, USA.

⁴Geospace and Earth Science Group, Space Department, The Johns Hopkins University Applied Physics Laboratory, Laurel, Maryland, USA.

Corresponding author: Joe Kinrade, Department of Electronic and Electrical Engineering, University of Bath, Bath, BA2 7AY, UK. (j.kinrade@bath.ac.uk)

total electron content (TEC) that are typically associated with geomagnetic storms and magnetospheric coupling events. The underlying mechanisms linking ionospheric structuring with specific GPS scintillation events are not fully understood; the high-latitude ionosphere can be extremely dynamic in space and time, and there may even be a combination or interplay of different physical mechanisms culminating in scintillation at the GPS receiver. One recent study has correlated many high-latitude scintillation measurements in a comprehensive inter-hemispheric conjugate study during a geomagnetic disturbance [Prikryl *et al.*, 2011]. The results indicate both symmetries and asymmetries in the ionospheric response and scintillation occurrence, demonstrating the complexities and dynamic nature of the physical mechanisms acting at high latitudes. It is accepted that seasonal axial tilt and asymmetry in the geomagnetic field render the Arctic and Antarctic ionospheres subject to different energy input and magnetospheric linkage for any given solar event.

[4] The majority of high-latitude Global Navigation Satellite System (GNSS) scintillation studies associated with auroral activity have been on a single case study basis. *Garner et al.* [2011] report a case of L2 signal loss associated with an auroral arc over Fairbanks, Alaska. *Smith et al.* [2008] observed, on multiple and closely sited GPS receivers, rapid signal fading and loss of GPS satellite lock associated with an optical arc and auroral precipitation over Norway during a geomagnetic substorm. Phase scintillation is more common at high latitudes. *Mitchell et al.* [2005] report phase scintillation on the edge of polar cap patches in the high European Arctic, and *Ngwira et al.* [2010] associate phase scintillation in the Antarctic with auroral electron precipitation. *Burston et al.* [2009] show evidence for both turbulence and the gradient drift instabilities being responsible for the production of electron density irregularities at high latitudes. *Kinrade et al.* [2011] observed moderate phase scintillation within the Antarctic dawn-noon sector, associated with E-region particle precipitation and the “break-off” point of a plasma enhancement patch into the Polar cap.

[5] Ionospheric irregularities are too small and dynamic to be imaged by most current inversion tomography methods; at high latitudes, they are typically associated with field-guided particle precipitation or the break-up of larger bodies of enhanced plasma density [Fejer and Kelley, 1980; Moen *et al.*, 1998]. Although advanced ionospheric imaging and data assimilation methods are now being applied effectively at high latitudes [Bust and Crowley, 2007; Kinrade *et al.*, 2011; Yin *et al.*, 2009], the achievable resolution of plasma morphology is limited by the density and distribution of the instruments and by the sparse nature of the inversion problem. The regional coverage of high latitude ground-based GNSS receivers has vastly improved over the last decade through active polar campaigns; however, the available ray path geometry only supports the reconstruction of large scale ionospheric features of hundreds of kilometers or more. Ionospheric irregularities are difficult to model or predict; they are usually only observed using ionospheric radars [Carlson, 2012]. Radio propagation models at high latitudes are only just beginning to account for ionospheric irregularities and scintillation [Strangeways, 2009].

[6] There is not a direct physical link between optical auroral emissions and ionospheric scintillation; photon release is a discrete energy product from the delayed relaxation of excited ions after collisional ionization. However, the optical emissions are to some extent local to the immediate area of ionization or radio aurora (this is dependent on the energy and flux of incoming particle precipitation, altitude and neutral densities present). This study examines the spatial and temporal correlation of ionospheric GPS scintillation with the intensity of optical auroral emissions. If a link can be quantified between the optical aurora and GPS scintillation, it may be feasible to use optical emissions as a proxy indicator of small-scale plasma structuring. The study of ionospheric irregularities and scintillation would benefit from a source of small-scale plasma observations.

2. Instruments and Method

2.1. GPS Scintillation Receiver

[7] The modified *Novatel GSV4004* GPS receiver tracks up to 11 satellites simultaneously at L1 (1575.42 MHz) and L2 (1227.60 MHz) frequencies, measuring phase and amplitude changes at a sample rate of 50 Hz. L1 amplitude and phase scintillation measurements are recorded in the form of the computed indices S_4 and σ_ϕ , respectively [Van Dierendock, 1999]. The receiver has a low-noise oscillator that can be used as a stable reference with which to measure the phase. The σ_ϕ index represents the average phase variance of the de-trended signal in radians within 60 s (3000 samples in time). Total Electron Content (TEC) is also computed using differential carrier phase and pseudorange measurements, but has not been used in this study.

[8] Observations made at low sky-view elevation angles ($<20^\circ$ above the local horizon) are removed to reject the most severe multipath. A cut-off minimum of 120 s continuous satellite contact or “lock” time is also required, accounting for the “settling” period of the receiver’s phase-locked tracking loop (PLL). This filtering stage provides a level of confidence that the measured scintillation parameters are representative of true ionospheric conditions, by minimizing the impact from the local multipath environment and systematic receiver effects.

2.2. South Pole All-Sky Imager (ASI)

[9] The ASI is located on the roof of the Amundsen-Scott South Pole Station, in close proximity to the true geographic South Pole; or 74.3° Corrected Geomagnetic Latitude (CGLAT) [Tanaka *et al.*, 2012]. The camera provides a temporal and spatial measure of optical auroral emission intensities within the central Antarctic plateau during the dark winter months [Ebihara *et al.*, 2007; Ejiri *et al.*, 1999]. The optics consists of a *Nikkor F1.4* aperture, 180° field-of-view “fish-eye” lens, projecting a wide angle image on to a CCD sensor of resolution 512×512 pixels. A rotating filter mechanism allows the capture of a range of images at discrete optical wavelength emissions, including atomic oxygen ([OI] 557.7 nm green line and [OI] 630.0 nm red line). Image exposure time is typically 4 s for both 557.7 nm and 630.0 nm emission intensities; images are recorded with a capture interval of ~ 24 s (image capture of

different emission wavelengths is interleaved in time as the filter mechanism rotates across the lens element). The intensity saturation point of the camera sensor for 557.7 nm emissions is ~ 44000 Rayleigh; the Rayleigh (R) is a photometric unit and is a measure of the rate of emission intensity or spectral radiance of spatially extended light-emitting sources [Baker, 1974]. Conversely, the sensitivity of the imager to low intensity emissions is dependent on instrument noise. The deviation of noise for the South Pole imager is ± 50 counts around the pixel value, corresponding to ~ 96 R at 630.0 nm, for a 4 s exposure. Taking the typical brightness of a low intensity emission such as airglow as 300 R [Hosokawa *et al.*, 2011], an image capture would have a signal-to-noise ratio of approximately 3. We expect that the detection of airglow would require dedicated longer exposures of more than 12 s, increasing the SNR to over 10. Some systematic corrections were applied to the “raw” images [Kubota *et al.*, 2001], including lens distortion correction, brightness uniformity adjustment, and compensation for atmospheric extinction and the Van Rhijn effect, the characteristic increase of observed emission intensity with increase in zenith angle towards the horizon [Chamberlain, 1961].

2.3. Image Processing and Satellite Tracking

[10] The optical images were mapped onto a geographic coordinate projection to facilitate the matching of scintillation measurements with optical image pixels using latitude/longitude pierce point positions. This required the assumption of

fixed altitude shells at 120 km and 200 km; these shell heights were chosen because they are characteristic of the most intense nightside 557.7 nm and 630.0 nm atomic oxygen emissions, respectively [Sandholt *et al.*, 2002]. Satellite-to-ground pierce points were calculated using GPS sp3 orbit file coordinates and intersection with the assumed emission altitudes. The mapping transform is demonstrated in Figure 1. A limitation of the instruments and method is that the image aspect represents the optical aurora from one position on the ground, i.e., at low elevation viewing angles, the ability to discern field-aligned structures is lost, and the intensity measurement represents an integral summation of the emissions. At the South Pole, the GPS constellation only provides elevation satellite coverage of up to $\sim 47^\circ$ above the horizon; however, the geometric projection of scintillation measurements on to 120 km and 200 km altitude shells somewhat constrains the observation area to the central portion of the topside-mapped and distortion-corrected images (where auroral arc or “curtain” features are still discernible). The use of multiple ground-based ASIs and/or topside satellite based optical instruments is required to better resolve small-scale structures over a large area.

[11] Each satellite pierce point, calculated using a fixed and assumed altitude shell, has an unknown level of uncertainty with regard to how closely it is matched with the true height of the optical emissions. This limitation motivated the statistical treatment of the images to improve conditions for spatial-based cross correlation with the GPS data and reduce pixel noise. Matrices of mean emission intensity were produced with one value representing each pixel for each

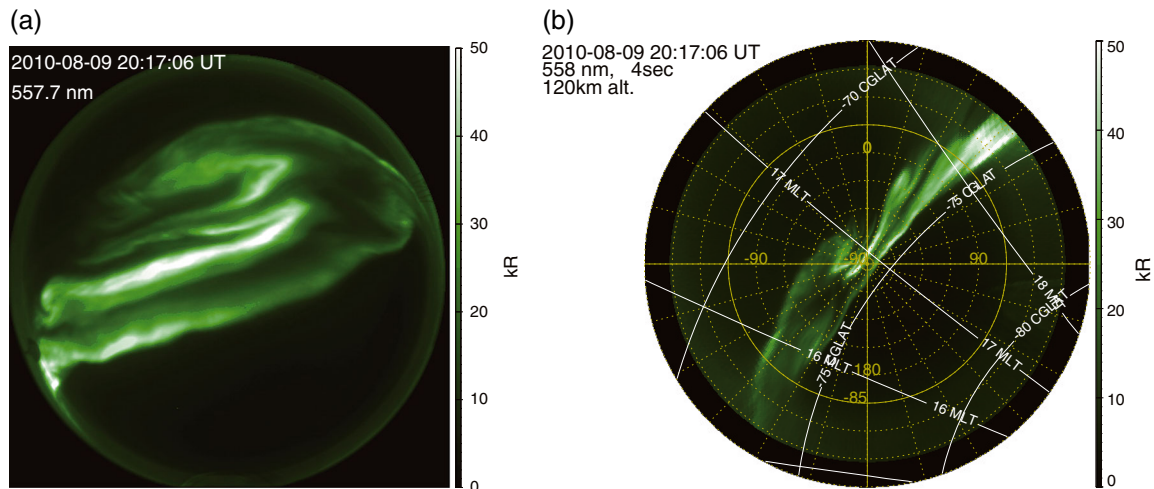


Figure 1. (a) An exemplary 557.7 nm emission image from the South Pole all-sky imager (ASI) on 9 August 2010 at 20:17:06 Universal Time (UT). The ASI is oriented so that the image appears as it would if the viewer was looking directly overhead (at the zenith) while stood at the geographic South Pole, with the Greenwich Meridian line passing vertically down the center of the image. The silhouette of the GPS antenna is just visible in the bottom-left edge of the image. Image processing is used to correct the images for wide-angle lens distortion and to map the pixels to the geographic coordinate system at shell heights of 120 km (557.7 nm emissions) and 200 km (630.0 nm emissions). (b) Image shows a corrected and pixel-mapped image, now orientated so that the viewer is looking from above (essentially how the aurora might appear from low-Earth orbit). Yellow lines indicate the geographic coordinate grid, with the majority of the useful image area falling within the latitude range $85\text{--}90^\circ$ S. The color-scale is in Rayleighs, a photometric unit, and applies to both Figures 1a and 1b.

time step by averaging each original pixel intensity value with respect to its surrounding pixels (± 5 pixels in the vertical and horizontal), i.e., a moving operator window. This process was also repeated to obtain “maximum” intensity images, taking the brightest value within the operator window. The use of these processed matrices (particularly the “maximum” values) in correlation with tracked GPS ray path measurements increases the likelihood of a scintillation event being matched correctly with smaller scale auroral emission structures such as wisps or curtains. Post processing, optical images have a pixel resolution of 200×200 , with each pixel space corresponding to an approximate physical dimension of 7.8 km—this dictates the lower limitation of scale for resolving structures within the processed images.

[12] Each scintillation measurement was time-matched with an optical image to within 1 min, with the closest image pixel position determined by calculating the least Euclidean distance between the orbit-derived latitude and longitude pierce point and the image coordinate grid (i.e., grid distance and not physical distance). A three-point moving

average filter was then also applied to the image pixels and scintillation measurements in time to improve conditions for cross correlation. By tracking multiple satellites in time and space, two collective time series result from the image processing; tracked emission intensities, $x_i(k)$, and phase scintillation measurements, $x_j(k)$. Correlation statistics were obtained directly from these two time series. The cross-correlation coefficient, R_{ij} , is related to the cross correlation, C_{ij} , by the following equations:

$$R_{ij} = \frac{C_{ij}}{\sqrt{C_{ii}C_{jj}}} \quad (1)$$

$$C_{ij} = \frac{1}{N-1} \sum_{k=1}^N (x_i(k) - \mu_i)(x_j(k) - \mu_j) \quad (2)$$

$$\mu_i = \frac{1}{N} \sum_{k=1}^N x_i(k) \quad (3)$$

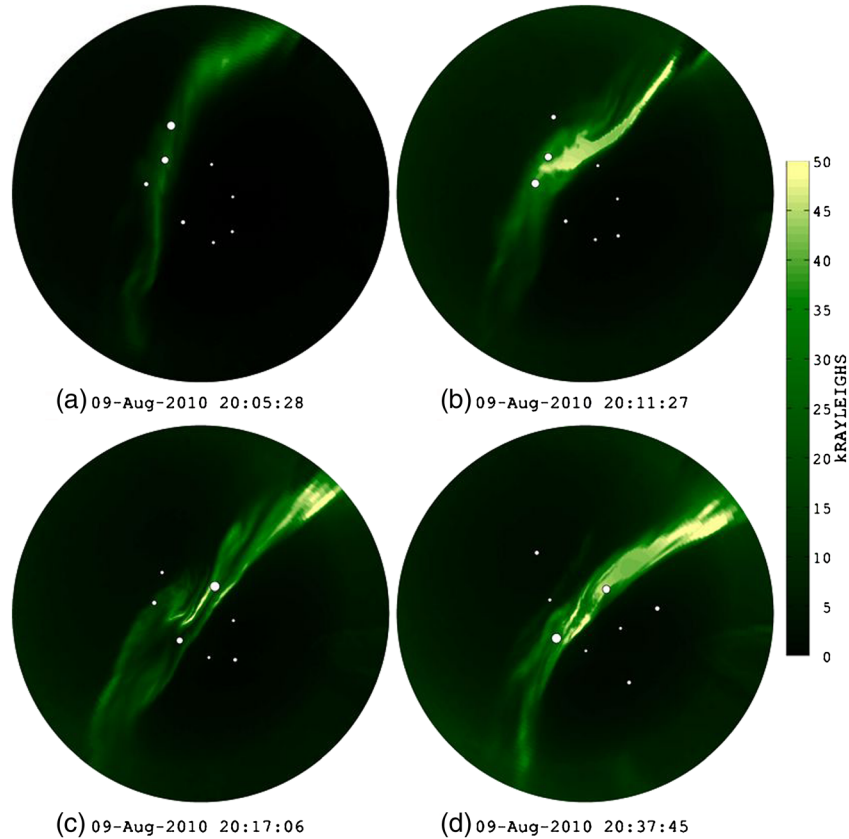


Figure 2. A selection of combined geographic projections of 557.7 nm emission intensity (kR) and GPS L1 phase scintillation indices ($60 \text{ s } \sigma_{\phi}$) at times (a) 20:05:28 UT, (b) 20:11:27 UT, (c) 20:17:06 UT, and (d) 20:37:45 UT on 9 August 2010 at South Pole. A common shell height of 120 km was assumed (characteristic of peak 557.7 nm atomic oxygen emissions on the nightside). The phase scintillation indices were plotted as area-scaled white circles, intended to highlight the apparent visual correspondence between signal phase variance and emission intensity at the pierce points; on visual inspection, the phase variance appeared to increase when the pierce point traversed brighter areas of emission. This relationship was most apparent when projections were viewed as a time-lapse animation. The color mapping of emission intensity used a black-green-yellow scale for clarity.

$$\mu_j = \frac{1}{N} \sum_{k=1}^N x_j(k) \quad (4)$$

[13] Accompanying visual plots depict the optical image with superimposed scintillation measurements from each tracked satellite (Figures 2 and 3 in section 3.1 are examples); the σ_ϕ values were plotted as area-scaled white circles, intended to highlight the apparent visual correspondence between signal phase variance and emission intensity at the pierce points.

[14] A total of 17 visible aurora days were selected for study from the Antarctic winters of 2010–2011, with activity ranging in intensity, duration, and structuring. Selection was on a visual basis, discounting images that captured the moon (an unwanted source of brightness that effectively masks the auroral emissions in an image) and favoring image sequences that displayed discrete or persistent auroral structuring. Correlation was performed at both wavelengths for each entire case study day (all satellites and all time samples available, Tables A1 and A2—Appendix A), and additionally over visually selected time intervals of pronounced auroral activity (Tables 2 and 3), ranging from discrete

auroral arcs to diffuse brightening. This visual selection sought to isolate “burst” periods, i.e., the entire lifetime of an arc or active period from formation to dissipation. By removing extended periods of “dark sky” from the time series, noise level image data were reduced and the statistics then represented more closely the relationship between the optical emissions and associated GPS phase fluctuations. The dates studied are listed in Tables A1 and A2 in Appendix A. Notable times of interest throughout these dates are listed in Tables 2 and 3. Summarized image sequences can be viewed online [Ebihara, 2007].

3. Results and Analysis

3.1. Discrete Auroral Arc—9 August 2010

[15] Of all the dates studied, the imagery of the auroral arc occurring over the Antarctic on 9 August 2010 displayed the most discrete and persistent optical activity. The imager recorded strong optical emissions (>40 kR) present during the times 1900–2200 Universal Time (UT). The arc spanned Magnetic Local Times (MLT) of 1600–1900 MLT at latitudes ~ 73 – 74° CGLAT. The duration and relatively stable magnetic position of the arc made it a useful candidate for tracking coincident scintillation “through” the optical

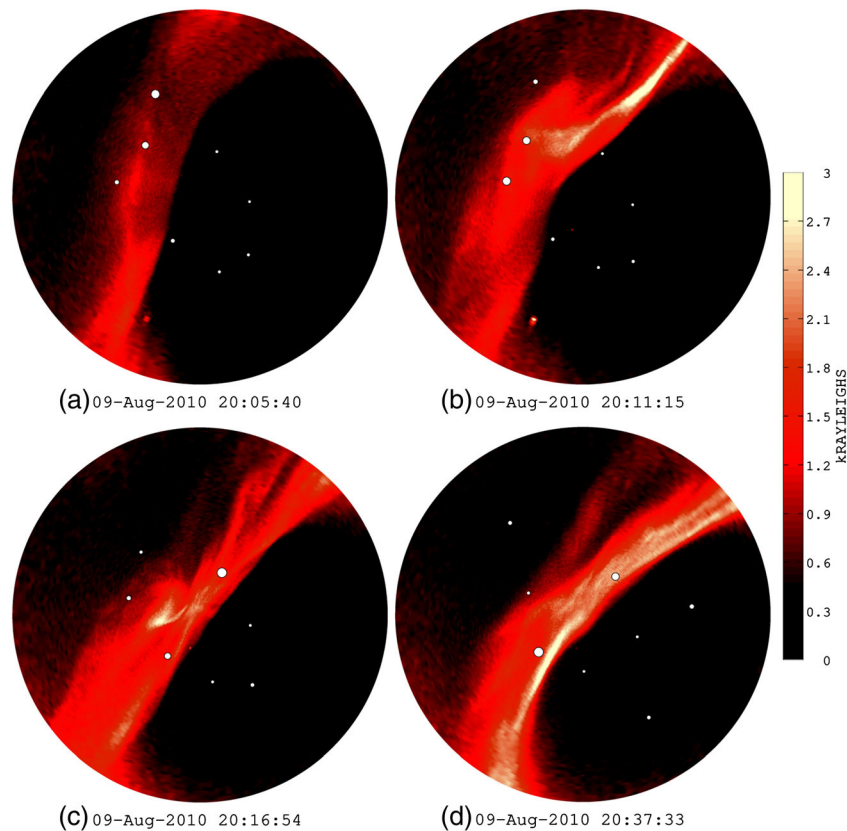


Figure 3. A selection of combined geographic projections of 630.0 nm emission intensity (kR) and GPS L1 phase scintillation indices (60 s σ_ϕ) at times (a) 20:05:40 UT, (b) 20:11:15 UT, (c) 20:16:54 UT, and (d) 20:37:33 UT on 9 August 2010 at South Pole. Note the generally lower intensity of the 630.0 nm emissions compared with those at 557.7 nm in Figure 2. An altitude shell height of 200 km was assumed (characteristic of peak 630.0 nm atomic oxygen emissions on the nightside). The color mapping of emission intensity used a black-red-yellow scale for clarity.

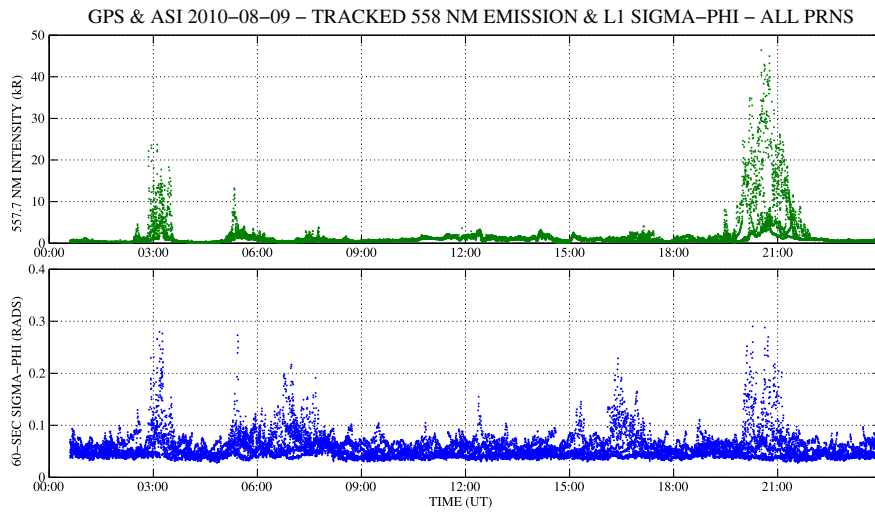


Figure 4. Two time series result from simultaneously tracking the observed satellites “through” the filtered ASI images; mean 557.7 nm emission intensities (top, green) and GPS L1 60 s σ_ϕ indices (bottom, blue) at 120 km pierce points coincident in space and time. Periods of auroral brightening can be seen here mainly around 0300 and 2000 UT on 9 August 2010, which matched well with “burst” periods of phase fluctuation. A smaller peak response was also present around 0500 UT. It is also important to note the occurrence of increased levels of phase fluctuation in the absence of optical emissions, during 1600–1700 UT here for example, when it is likely that a different physical mechanism was responsible for the ionospheric irregularities affecting L1 signal propagation, or that particle precipitation was predominant at a different altitude at that time (see Figure 5).

images, and illustrating the method as the first case study here. Figures 2 and 3 provide a selection of geographic projections of 557.7 nm and 630.0 nm emission intensities and GPS L1 phase scintillation indices, respectively, illustrating their visual correspondence—this was readily observed when the images were viewed in time-lapse animation.

[16] Two time series result from simultaneously tracking the observed satellites “through” the filtered ASI images; Figure 4 shows the collective satellite mean 557.7 nm intensity and σ_ϕ fluctuations on 9 August 2010. Periods of auroral brightening can be seen mainly around 0300 UT and 2000 UT, which matched well with “burst” periods of phase

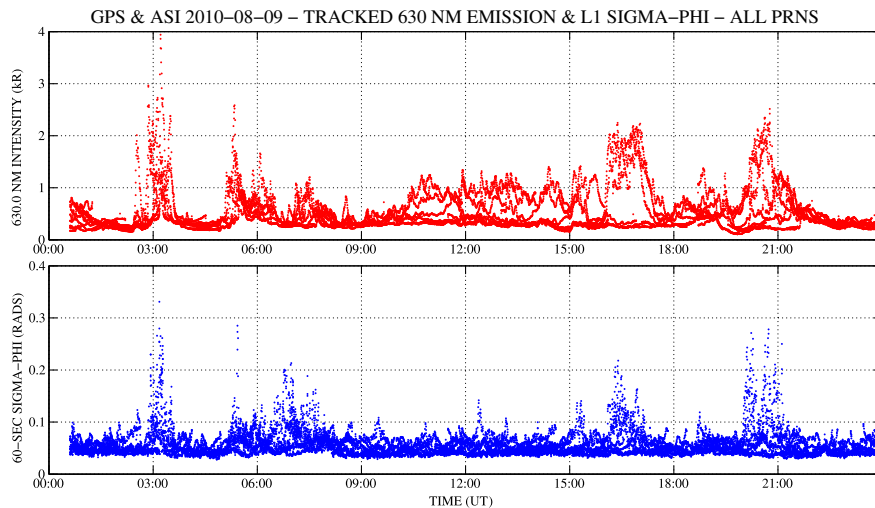


Figure 5. Tracked mean 630.0 nm emission intensities (top, red) and GPS L1 60 s σ_ϕ indices (bottom, blue) at 200 km pierce points during 9 August 2010. The 630.0 nm emissions are characteristically less intense compared with those at 557.7 nm (see Figure 4); however, the two time series do display a general visual correspondence between optical and phase fluctuation “bursts.” In addition to the optical activity imaged around 0300 UT and 2000 UT (also at 557.7 nm in Figure 4), other instances of correlation may be inferred at 0500 UT and 1600–1700 UT. Interestingly, the phase fluctuations between 1600–1700 UT appear to be associated with 630.0 nm emissions at 200 km, but not 557.7 nm at 120 km (see Figure 4), indicating that the ionization structuring existed nearer the F-region during the period.

fluctuation. A smaller peak response was also present around 0500 UT. It is also important to note the occurrence of increased levels of phase fluctuation in the absence of optical emissions at this wavelength, during 1600–1700 UT for example, when it is likely that either a different physical mechanism was responsible for the ionospheric irregularities affecting L1 signal propagation (see section 3.2), or that particle precipitation was predominant at a different altitude at that time. Comparison of the tracked time series at dual emission wavelengths allows a basic level of altitude discrimination. Figure 5 shows the tracked 630.0 nm time series on 9 August 2010. Referring to Figures 4 and 5, the phase fluctuations between 1600–1700 UT appear to be associated with 630.0 nm emissions at 200 km, but not 557.7 nm at 120 km, indicating that the responsible ionization structuring was nearer the F-region at the time. This is a significant finding, as it supports the possible use of multiple-wavelength auroral images to determine both the sky area of likely scintillation conditions, and the approximate altitude of the driving ionization. Polar cap ionization patches have been observed to exhibit low intensity (100–500 R) [OI] red 630.0 nm emissions at F-region altitudes [Garner *et al.*, 1996], however this level of brightness is close to the ASI noise threshold in the context of this experiment, particularly for the weaker 630.0 nm emission line, as discussed in section 2.2. Detection of polar cap patch-related emissions can be improved by

increasing image exposure times and is an interesting aspect of planned future work.

[17] This illustrative case study provides clear evidence that regions of intense auroral optical emissions can be

Table 1. Selected 557.7 nm and 630.0 nm Correlation Statistics During 1900–2200 UT on 9 August 2010^a

PRN ^b	No. data points	R_{558}	R_{LO}	R_{UP}
32	180	0.8875	0.8518	0.9150
20	251	0.8723	0.8391	0.8990
31	429	0.8105	0.7754	0.8407
23	340	0.6262	0.5569	0.6868
4	392	0.6260	0.5618	0.6827
30 ^c	385	-0.0534	-0.1525	0.0468
		R_{630}		
31	179	0.7530	0.7089	0.7913
32	251	0.7431	0.6693	0.8023
20	429	0.6403	0.5609	0.7080
4	340	0.5747	0.5043	0.6374
23	392	0.5738	0.4978	0.6411
30	384	0.2445	0.1480	0.3363

^a R_{558} is the linear cross-correlation coefficient between mean 557.7 nm emission intensity and σ_ϕ indices at 120 km altitude. R_{630} is the linear cross-correlation coefficient between mean 630.0 nm emission intensity and σ_ϕ indices at 200 km altitude. R_{LO} and R_{UP} are the lower and upper 95% confidence limits of the correlation coefficient, respectively.

^bPseudo Random Noise (PRN) satellite code.

^cPRN 30 displayed little phase variation during the auroral arc event, and its ray paths did not traverse the auroral arc at 120 km; its inclusion serves to show a typical 557.7 nm noise-floor correlation level.

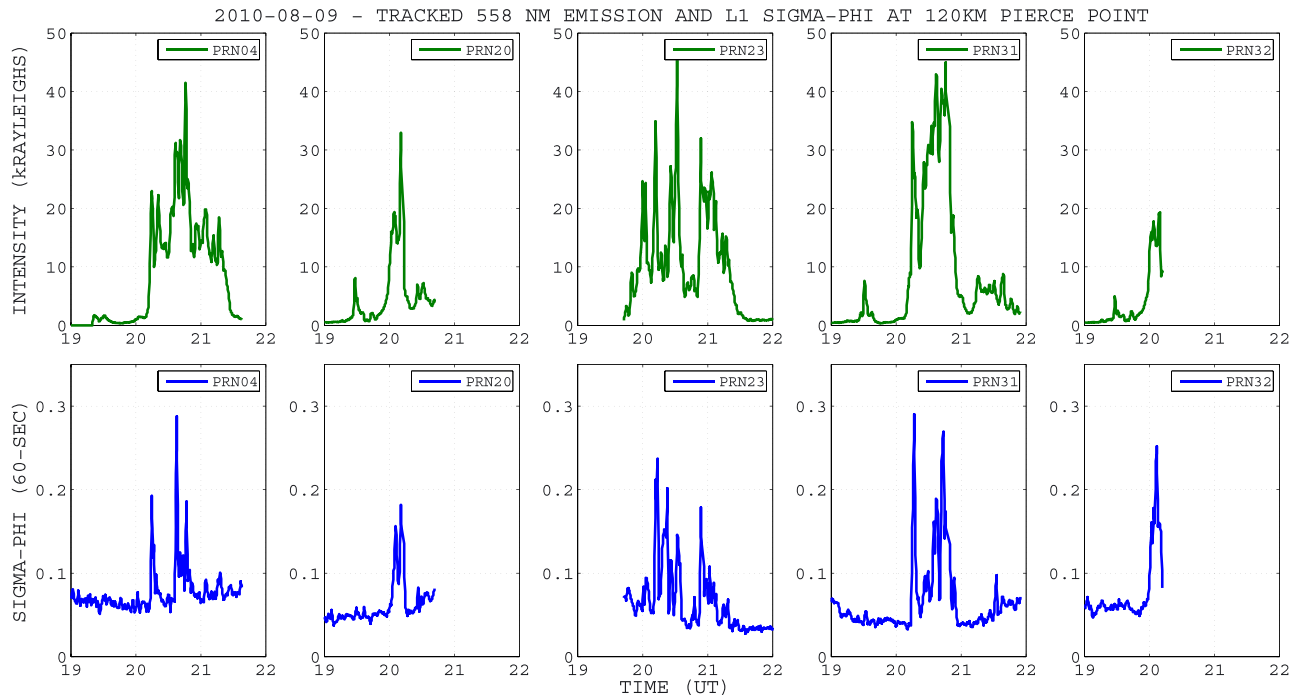


Figure 6. Selected satellite-tracked time series of GPS L1 phase scintillation indices (bottom row) and mean 557.7 nm emission intensities (top row) at 120 km, during 1900–2200 UT on 9 August 2010. Although only moderate levels of phase scintillation were observed (<0.3 rad), examining a “burst” period on a satellite-by-satellite basis reveals that a number of tracked satellites exhibited peak signatures in σ_ϕ coincident with enhancements in local 557.7 nm emission intensity. Table 1 lists the cross-correlation coefficients for these satellite tracks.

Table 2. Collective-Satellite 557.7 nm Correlation Coefficients^a

Date	Time Span (UT)	No. Data Points	R ₅₅₈	R _{LO}	R _{UP}	Max. σ_ϕ	Max. I _{max}
2011-07-31	2202–2359	1842	0.7421	0.7209	0.7620	0.5628	50828
2010-08-09	1901–2200	3337	0.6871	0.6688	0.7046	0.2902	50457
2010-05-21	0001–0300	3266	0.6423	0.6217	0.6620	0.5248	49791
2011-05-26	0002–0115	1362	0.6402	0.6077	0.6705	0.4814	51688
2011-04-30	2031–2130	636	0.6048	0.5531	0.6519	0.5049	49697
2011-05-04	0002–0215	2465	0.6030	0.5773	0.6276	0.5698	3220
2011-05-03	0002–0159	2083	0.5854	0.5565	0.6310	0.4121	46179
2011-05-02	0003–0130	1154	0.5785	0.5388	0.6157	0.5988	46730
2010-08-03	0000–0130	1724	0.5761	0.5437	0.6068	0.4071	20584
2010-06-16	0041–0359	3497	0.5662	0.5432	0.5883	0.4166	36075
2010-05-20	0146–0330	1931	0.5256	0.4926	0.5572	0.4098	49920
2010-08-09	0201–0900	7477	0.4853	0.4678	0.5024	0.2796	40348
2011-07-25	0002–0630	6824	0.4375	0.4181	0.4565	0.3254	17514
2011-05-28	0003–1130	6346	0.4371	0.4170	0.4568	0.4459	10138
2011-05-03	1702–2159	5495	0.4290	0.4072	0.4503	0.2556	40119
2011-05-01	0003–0259	2675	0.3978	0.3654	0.4292	0.3146	35219
2010-08-04	0016–0130	1219	0.3366	0.2858	0.3854	0.6109	18318
2011-05-03	1102–1359	3170	0.1775	0.1436	0.2110	0.6141	43775
2011-05-01	0831–0859	428	0.0578	−0.0372	0.1518	0.2882	46374
2011-05-01	1603–2359	7214	0.0323	0.0093	0.0554	0.5248	36243

^aCollective-satellite correlation coefficients during notable periods of optical auroral activity, using maximum intensity 557.7 nm emission images. Peak values of σ_ϕ indices and emission intensity, I_{max}, from all observed satellites in the time interval are provided for reference.

associated with GPS phase fluctuations. During the discrete arc event on 9 August 2010, examination of the tracked time series on an individual satellite basis (see Figure 6) revealed spatial and temporal 557.7 nm correlations of between 62–89% at 120 km altitude over the three-hour period 1900–2200 UT (see Table 1). During the same period, emissions at 630.0 nm also correlated between 24–75% on an individual satellite basis at 200 km (Table 1). The collective satellite correlation during this period was 69% for 557.7 nm emissions at 120 km and 57% for 630.0 nm emissions at 200 km (see Tables 2 and 3). Additionally, statistical *p*-values indicated that the probability of these correlation levels occurring through random chance was practically zero. The proxy relationship between the

auroral emissions and GPS phase fluctuations was therefore statistically significant.

3.2. Other Sources of Scintillation at High Latitudes

[18] It is important to acknowledge that other physical mechanisms causing scintillation can exist at high latitudes, notable during a number of days in this study. Evidence of this is pronounced in Figure 7, which compares tracked time series from 557.7 nm to 630.0 nm optical emissions with σ_ϕ on 28 May 2011. Optical emissions were generally of weak intensity during this day (<10 kR at 557.7 nm, <4 kR at 630.0 nm), although peak signatures did correspond spatially and temporally with phase fluctuations up until 1200 UT at both wavelengths (~0200 UT at 557.7 nm, for example). After

Table 3. Collective-Satellite 630.0 nm Correlation Coefficients^a

Date	Time Span (UT)	No. Data Points	R ₆₃₀	R _{LO}	R _{UP}	Max. σ_ϕ	Max. I _{max}
2011-07-31	2202–2359	1821	0.6253	0.5965	0.6525	0.5628	3646.1
2010-06-16	0041–0400	3498	0.5791	0.5567	0.6007	0.4543	3789.9
2010-05-20	0146–0330	1921	0.5765	0.5458	0.6056	0.3480	5246.8
2010-08-09	1901–2200	3339	0.5745	0.5513	0.5968	0.2780	4350.5
2011-05-03	0002–0159	2072	0.4937	0.4604	0.5256	0.4358	3734.8
2010-08-04	0016–0130	1227	0.4846	0.4406	0.5263	0.6109	5512.9
2011-07-25	0002–0630	6776	0.4809	0.4624	0.4990	0.3410	5134.2
2010-08-09	0201–0900	7470	0.4679	0.4500	0.4854	0.3310	5179.0
2011-05-01	0002–0259	5102	0.4665	0.4448	0.4877	0.3993	4274.7
2011-05-28	0002–1130	6344	0.4642	0.4447	0.4833	0.4459	4861.3
2011-04-30	2031–2130	1270	0.4393	0.3938	0.4826	0.5049	5643.2
2011-05-04	0002–0215	2441	0.4084	0.3748	0.4410	0.5247	2410.9
2011-05-01	1602–2359	13802	0.3966	0.3825	0.4106	0.5512	6286.6
2011-05-03	1102–1359	3179	0.3923	0.3625	0.4213	0.4828	3515.0
2011-05-03	1702–2159	5497	0.3871	0.3643	0.4093	0.2849	4223.7
2010-05-21	0001–0300	3277	0.3600	0.3298	0.3894	0.6034	3505.4
2010-08-04	1031–1645	6630	0.3544	0.3331	0.3752	0.5360	3625.1
2010-08-03	0001–0130	1744	0.3450	0.3030	0.3857	0.4071	1989.7
2011-05-02	0002–0130	2312	0.3118	0.2745	0.3481	0.5988	5197.4
2011-04-30	0831–1630	13634	0.2889	0.2734	0.3042	0.5473	7663.8
2011-05-01	0831–0859	738	0.0799	0.0078	0.1512	0.3101	3519.3

^aAs for Table 2, but using maximum intensity 630.0 nm images.

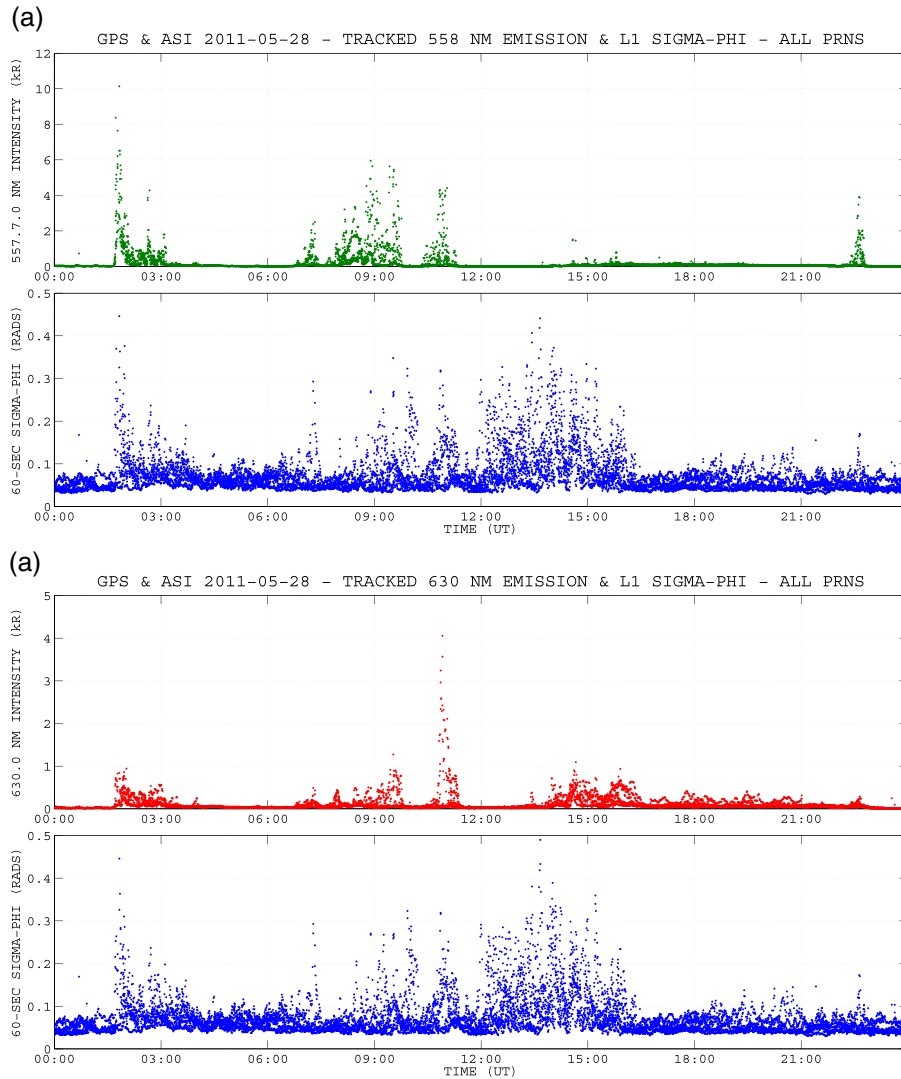


Figure 7. (a) Tracked 557.7 nm and (b) 630.0 nm mean emission intensities and GPS L1 σ_{ϕ} indices on 28 May 2011. Although emission intensities were relatively weak throughout the day, peak signatures in emission brightness and moderate phase fluctuation did coincide at both wavelengths until ~ 1200 UT, more so at 557.7 nm. After 1200 UT, however, a prolonged period of phase fluctuation ensued for \sim four hours across the majority of observed satellites, which was not associated with optical activity at the wavelengths observed; emission intensity values were minimal and near the image noise floor. It is likely that another physical mechanism was acting within the signal propagation environment throughout that time to cause the phase fluctuations.

1200 UT, however, a prolonged period of phase fluctuation ensued for \sim four hours across the majority of observed satellites, which was not associated with pronounced optical activity at the wavelengths observed; emission intensity values were minimal and near the image noise floor. It is likely that another physical mechanism was present within the signal propagation environment throughout that time and other similar days in the study. Image reconstructions of Total Electron Content (TEC) indicated the presence of larger scale ionospheric electron density gradients over central Antarctica for a number of hours after 1200 UT on 28 May 2011 (TEC images were produced using the GPS inversion tomography tool MIDAS [“Multi-Instrument Data Analysis System” created by Mitchell and Spencer, 2003, and described in Chartier et al., 2012]). In addition to the auroral

precipitation processes of interest in this optical study, possible sources of high latitude phase scintillation include electron density irregularities driven by polar cap patch convection [Buchau et al., 1985; Burston et al., 2009; Mitchell et al., 2005].

3.3. Cross-Correlation Statistics

[19] Collective cross-correlation statistics offer a numerical overview of the case studies, important in identifying any proxy relationship between the optical auroral emissions and GPS phase scintillation. The statistics reveal that the proxy relationship between optical auroral emissions and GPS σ_{ϕ} was variable over the Antarctic winter days studied. Images at 557.7 nm and 630.0 nm correlated collectively

with GPS phase fluctuations to levels ranging 03–74% and 08–63%, respectively. Images exhibiting diffuse and finely structured auroral emissions have generally produced lower levels of collective satellite σ_ϕ correlation. Taking an example, the optical auroral activity throughout the day of 1 May 2011 consisted of a mixture of diffuse brightening and dynamic wisps. A bright and filamentary wisp structure was imaged during 0830–0900 UT (>40 kR intensity), but collective satellite σ_ϕ correlation was only 6% and 8% at green and red wavelengths, respectively (see Tables 2 and 3). This type of “fine” structuring has less spatial clarity and longevity than discrete arcs or curtains, and so the numerical outcome of the cross correlation is more sensitive to the simplifications made in the method—namely spatial image filtering, data point time matching, and the use of altitude shell heights in pierce point determination. Consider also that the energy and flux of field-guided particle precipitation influence the rate of direct ionization and subsequent intensity of auroral emissions; it follows that discrete and persistent arc structures are likely associated with more pronounced local electron density gradients and therefore GPS scintillation, in comparison with the impulsive and weaker intensity emissions of diffuse or wisp aurorae. Additionally, time series from a number of days in the study exhibited periods of phase fluctuation likely associated with physical processes other than direct auroral ionization, as discussed in section 3.2. Correlation on affected ray paths is therefore likely to have been poor, leading to lower collective correlation values.

[20] Periods of intense and persistent optical activity produced the strongest σ_ϕ correlation statistics of the study. Discrete auroral arc structures were imaged on several days (notably 9 August 2010 and 31 July 2011), with emission

intensities that occasionally saturated the ASI sensor (~ 44 kR for green 557.7 nm emissions). Over a two-hour period on 31 July 2011, the green and red auroral emissions correlated with collective GPS L1 σ_ϕ measurements to levels of 74% and 63%, respectively. Over a three-hour period on 9 August 2010, the green and red emission correlation levels were 69% and 57%, respectively, with individual ray path fluctuations correlating with green emissions at up to 89% (PRN 32, see Table 1). Of the selected 557.7 nm image sequences examined, 15 out of 20 cases displayed collective σ_ϕ correlation above 40% (see Table 2). Of the selected 630.0 nm image sequences examined, 12 out of 21 cases displayed collective σ_ϕ correlation above 40% (see Table 3). A correlation level of 40% between observables is an arbitrary reference point here, however, the time series and image animations were often more suggestive of a physical relationship than the numerical statistics. As already noted, auroral behavior and GPS phase scintillation are both spatially and temporally dynamic on multiple scales, and so considering the tracking method’s limitations and assumptions, the statistics support a proxy relationship between optical emissions and σ_ϕ in the presence of strong auroral activity. Stronger statistics may be recoverable through the refinement of applied shell heights and spatial image filtering, and an increased focus on individual satellite tracks (additionally high time resolution 50 Hz GPS phase data can help to determine the nature of the physical mechanism causing scintillation, a method to be applied in a future study).

[21] The collective statistics suggest that the 557.7 nm emissions are more closely associated with phase fluctuations than those at 630.0 nm (see Tables 2 and 3). This is likely due to the relative intensity of the green and red optical aurorae, as the green emissions are characteristically a factor greater than red emissions. The

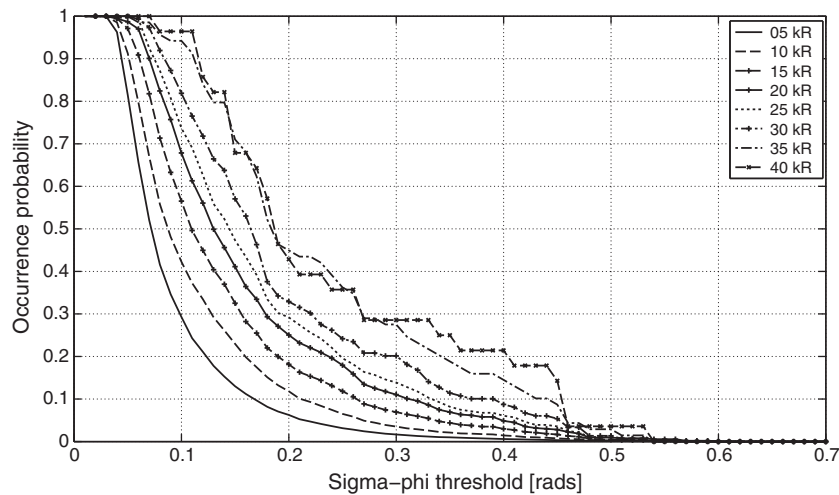


Figure 8. General trend interpretation of the relationship between 557.7 nm emission intensity and GPS phase scintillation indices, incorporating data from all case study days and tracked satellites ($\sim 300,000$ data points). The plot shows the conditional occurrence probability of the σ_ϕ index being above a certain value, given a coincident emission intensity threshold at the tracked pierce point; a number of fixed intensity threshold values were used in the calculation, ranging from 5 to 40 kR, with the σ_ϕ threshold stepped through values 0.0–0.7 rad for each case. For example, considering all pierce points in the study that intersected 557.7 nm auroral emissions of intensity 40 kR and over, $\sim 30\%$ of the corresponding σ_ϕ indices were over 0.3 rad. In summary and based on data from this study, the likelihood of σ_ϕ fluctuation along a ray path increases with higher intensity 557.7 nm emissions around the pierce point.

imaged structures are therefore more pronounced from the background image noise, and the tracking method is more effective. Note that the 630.0 nm emission lifetimes are characteristically longer than those of the 557.7 nm emissions [Sandholt *et al.*, 2002]; this may also reduce the correlation coefficient of the red time series. Although the use of dual wavelengths facilitates altitude discrimination (see Section 3.2), the 557.7 nm images would be the most suitable primary wavelength to examine if the ASI images were to be used to estimate sky-wide GPS scintillation activity.

3.4. On the σ_ϕ/I_{558} Proxy Relationship as a General Trend

[22] From an operational perspective, it would be useful to confirm a general relationship between auroral emissions and GPS signal disturbances, and whether there is a particular intensity threshold above which auroral emissions are more likely to be coincident with GPS phase scintillation. This knowledge would aid the systematic analysis of auroral images for determining the likelihood and sky location of scintillation activity. Figure 8 summarizes the collective case study (~300,000 data points) probability of the phase scintillation index being above a certain value for a range of 557.7 nm emission intensity (I_{558}) thresholds. This was calculated by summing both the number of occurrences of the optical emission values being above the stated intensity threshold, and the number of occurrences of the σ_ϕ index being above a threshold given the prior emission intensity condition. The sum of σ_ϕ occurrences was then divided by the sum of the emission intensity occurrences, yielding the rate of occurrence of scintillation “events” during auroral emission “events”. Appendix B provides a mathematical summary of this calculation. There are no universally accepted threshold values for either GPS phase scintillation activity (although a σ_ϕ value of 0.3 rad is often used in the literature) or the defining 557.7 nm intensity level of a discrete auroral emission structure, but interpretation of the data set in this way has revealed a general trend—higher values of emission intensity corresponded with more elevated levels of σ_ϕ index (see Figure 8). For example, considering all pierce points in the study that intersected 557.7 nm auroral emissions of intensity 5 kR and over, of those instances, ~30% of the corresponding σ_ϕ indices were above the near noise floor of 0.1 rad. Increasing the emission “event” intensity threshold to 30 kR showed that ~80% of σ_ϕ values during relatively bright emissions were above 0.1 rad.

4. Conclusions and Summary

[23] First, results have been presented from an experimental setup at the geographic South Pole using a collocated all-sky imager (ASI) and GPS scintillation receiver, investigating the usability of optical emission images as a proxy indicator of ionization structuring due to particle precipitation in the Antarctic. A collection of auroral events during Antarctic winters in 2010 and 2011 has been examined. This is the first time that multi-wavelength optical emission images have been compared with scintillation measurements in this way, including the high altitude red aurorae (atomic oxygen 630.0 nm line at 200 km).

Importantly, the study has yielded the first statistical evidence highlighting the previously assumed relationship between the aurorae and GPS signal propagation. The observation of dual wavelengths facilitates a useful level of height discrimination in determining the altitude of the direct ionization causing phase scintillation.

[24] The study sought to answer the fundamental question: “when we observe auroral optical emissions overhead, does a GPS receiver experience signal phase fluctuations from ray paths traversing those emissions?” This proxy relationship was found to be variable, and dependent on auroral intensity and structure definition. Spatial and temporal correlation with σ_ϕ was most defined during intense and persistent optical auroral activity, notably during the presence of discrete auroral arcs; correlation levels of up to 74% and 63% were found at the atomic oxygen 557.7 nm and 630.0 nm wavelengths, respectively (with statistical p -values of zero). From Tables 2 and 3, it may be observed that the majority of optical auroral activity in the study occurred around magnetic midnight and then at magnetic dusk, when it is likely that South Pole Station was positioned around the poleward boundary of the auroral oval. Correlation was generally lower during periods of diffuse aurorae and dynamic wisp structuring as the statistical outcome became more sensitive to limitations of the tracking method. It is expected that the stronger the emission intensity, the higher the rate of local recombination and therefore likelihood of scintillation-producing irregularities. In general, the 557.7 nm emissions correlated more closely with σ_ϕ than those at 630.0 nm, but this was likely due to the tracking method’s effectiveness at two emission wavelengths of different characteristic intensity. Refinement of assumed altitude shells and spatial and temporal image filtering might help to improve the cross-correlation statistics in future applications, and increased image exposure times would allow better detection of low level 630.0 nm emissions associated with polar cap patch irregularities. A conditional probability analysis of all data points revealed a general trend, namely those higher values of emission intensity corresponded with more elevated levels of σ_ϕ index. An increased focus on individual satellite tracks for specific auroral events is a useful development in terms of understanding the physical mechanisms present when a GPS receiver is experiencing scintillation.

[25] Amplitude fading has not been investigated here, as general levels of the S_4 index (based on a normalized average of the signal carrier-to-noise power) appeared low on initial inspection. Smith *et al.* [2008] showed that analysis of the signal sampled at 50 Hz is generally required for observing the short duration signal fading associated with auroral arcs at high latitudes. The moderate levels of phase scintillation observed in this case study (σ_ϕ up to ~0.6 rad) were not sufficient to cause any significant signal tracking problems for the GPS scintillation receiver. An upcoming study will examine high temporal resolution GPS phase data (50 Hz) to help determine the physical source of the scintillation during optical auroral events. In conclusion, optical images of the aurorae from the South Pole have shown to be a useful spatial and temporal indicator of GPS phase scintillation during intense and persistent auroral activity, most notably in the presence of discrete arcs at the auroral boundary.

Appendix A: Additional Correlation Statistics

Table A1—All Available Data—Collective-Satellite 557.7 nm Correlation Coefficients^a

Date	Time Span (UT)	No. Data Points	R ₅₅₈	R _{LO}	R _{UP}	Max. σ_ϕ	Max. I_{mean}
2010-06-16	0041–0359	3497	0.5525	0.5290	0.5751	0.4166	23482
2010-08-03	0000–0200	2335	0.5487	0.5197	0.5764	0.4071	15805
2011-07-31	0002–2359	25582	0.5323	0.5235	0.5411	0.5628	48416
2010-05-21	0001–0000	25299	0.4933	0.4839	0.5026	0.5248	36883
2010-08-09	0037–0000	25670	0.4358	0.4259	0.4457	0.2902	46384
2010-05-20	0013–0000	25911	0.2986	0.2874	0.3096	0.4098	31246
2011-05-26	0002–2359	25777	0.2912	0.2800	0.3023	0.4814	44720
2011-05-02	0003–0659	5991	0.2474	0.2235	0.2711	0.5988	32484
2011-05-03	0002–2359	25884	0.2382	0.2267	0.2497	0.6141	32765
2011-05-28	0003–2359	13376	0.2332	0.2171	0.2491	0.4459	10138
2011-04-29	1803–1959	1790	0.2208	0.1762	0.2644	0.2773	6651
2011-07-25	0002–2359	25545	0.1763	0.1644	0.1882	0.3584	8394
2011-04-28	1602–2359	4826	0.1536	0.1259	0.1810	0.3110	24021
2011-04-30	0003–2359	20568	0.1351	0.1217	0.1485	0.5201	46117
2010-08-04	0000–1601	17064	0.0686	0.0537	0.0836	0.6109	16579
2011-05-04	0002–2359	26280	0.0058	−0.0063	0.0179	0.5698	18657
2011-05-01	0003–2359	21747	−0.0149	−0.0282	−0.0017	0.6318	23428

^aCollective-satellite correlation coefficients resulting from the complete ASI datasets for the case study days (all available times), using mean intensity 557.7 nm emission images. R_{LO} and R_{UP} are the lower and upper 95% confidence limits of the correlation coefficient, respectively. Peak values of σ_ϕ indices and emission intensity, I_{mean} , from all observed satellites in the time interval are provided for reference.

Table A2—All Available Data—Collective-Satellite 630.0 nm Correlation Coefficients^a

Date	Time Span (UT)	No. Data Points	R ₆₃₀	R _{LO}	R _{UP}	Max. σ_ϕ	Max. I_{mean}
2010-06-16	0041–0440	4250	0.5947	0.5749	0.6138	0.4543	3002.3
2010-08-09	0037–0000	25673	0.4936	0.4843	0.5028	0.3310	3940.5
2010-05-20	0013–0000	25913	0.4582	0.4485	0.4678	0.3480	5713.1
2011-04-30	0002–2359	41330	0.4336	0.4258	0.4414	0.5473	5646.1
2011-05-03	0002–2359	25883	0.4114	0.4012	0.4215	0.4828	3167.5
2011-05-28	0002–0000	13360	0.3911	0.3766	0.4054	0.4896	4056.6
2010-08-03	0001–0336	4291	0.3873	0.3615	0.4124	0.4071	1737.0
2011-07-25	0002–2359	25357	0.3857	0.3752	0.3962	0.3584	4274.6
2010-08-04	0001–0000	25479	0.3638	0.3531	0.3744	0.7310	5124.9
2011-05-01	0002–2359	41431	0.3576	0.3492	0.3660	0.6318	3826.1
2011-07-31	0002–2359	25406	0.3446	0.3338	0.3554	0.5628	2830.9
2011-05-02	0002–0659	12012	0.3405	0.3246	0.3562	0.5988	3179.7
2011-04-29	0002–2033	35852	0.3243	0.3150	0.3335	0.4770	3720.5
2010-05-21	0001–0000	25309	0.3167	0.3056	0.3278	0.6034	3005.8
2011-05-04	0002–2359	26267	0.2292	0.2177	0.2406	0.5247	2190.0
2011-04-28	0002–2359	14756	0.2261	0.2107	0.2413	0.3466	3050.2
2011-05-26 ^b	0002–2359	25594	−0.0030	−0.0152	0.0093	0.3792	53.6

^aCollective-satellite correlation coefficients resulting from the complete ASI datasets for the case study days (all available times), using mean intensity 630.0 nm emission images. R_{LO} and R_{UP} are the lower and upper 95% confidence limits of the correlation coefficient, respectively. Peak values of σ_ϕ indices and emission intensity, I_{mean} , from all observed satellites in the time interval are provided for reference.

^bNote that 630.0 nm emission images were at noise level throughout the day of 26 May 2011.

Appendix B: Conditional Occurrence Probability

[26] Applying threshold values I_{TH} and S_{TH} to optical 557.7 nm emission intensity (I_{558}) measurements and GPS σ_ϕ indices, respectively:

[27] $P(S|I)$ is the conditional probability of a σ_ϕ event given an I_{558} event, where:

$$S = \text{an event defined by } \sigma_\phi \geq S_{\text{TH}}$$

$$I = \text{an event defined by } I_{558} \geq I_{\text{TH}}$$

[28] This was calculated from the entire study dataset by

$P(S|I) = n(S|I)/n(I)$, where:

$n(S|I)$ = total number of occurrences of both S and I events

$n(I)$ = total number of occurrences of I events

[29] **Acknowledgments.** Thanks to Dr. Biagio Forte (University of Bath, UK) and Dr. Ping Yin (Civil Aviation University of China) for their helpful insights. Logistic fieldwork support was provided by the British Antarctic Survey (BAS, Cambridge, UK) and the National Science Foundation (NSF). JK's PhD studies are supported by the Engineering and Physical Sciences Research Council (EPSRC) and the Isle of Man Government. CNM acknowledges support from the Royal Society Wolfson Award.

References

- Baker, D. (1974), Rayleigh, the unit for light radiance, *Appl. Opt.*, *13*(9), 2160–2163, doi:10.1364/AO.13.002160.
- Buchau, J., E. J. Weber, D. N. Anderson, H. C. Jr. Carlson, J. G. Moore, B. W. Reinisch, and R. C. Livingston (1985), Ionospheric structures in the polar cap: Their origin and relation to 250-MHz scintillation, *Radio Sci.*, *20*(3), 325–338, doi:10.1029/RS020i003p00325.
- Burston, R., I. Astin, C. Mitchell, L. Alfonsi, T. Pedersen, and S. Skone (2009), Correlation between scintillation indices and gradient drift wave amplitudes in the northern polar ionosphere, *J. Geophys. Res.*, *114*, A07309, doi:10.1029/2009JA014151.
- Bust, G. S., and G. Crowley (2007), Tracking of polar cap ionospheric patches using data assimilation, *J. Geophys. Res.*, *112*, A05307, 1–17, doi:10.1029/2005JA011597.
- Carlson, H. C. (2012), Sharpening our thinking about polar cap ionospheric patch morphology, research, and mitigation techniques, *Radio Sci.*, *47*, RS0L21, doi:10.1029/2011RS004946.
- Chamberlain, J. W. (1961), Spectral photometry of the nightglow, in *Physics of the Aurora and Airglow*, Academic Press Inc., New York & London.
- Chartier, A. T., C. N. Mitchell, and D. R. Jackson (2012), A 12 year comparison of MIDAS and IRI 2007 ionospheric total electron content, *Adv. Space Res.*, *49*(9), 1348–1355, doi:10.1016/j.asr.2012.02.014.
- Dahlgren, H., A. Aikio, K. Kaila, N. Ivchenko, B. S. Lanchester, D. K. Whiter, and G. T. Marklund (2010), Simultaneous observations of small multi-scale structures in an auroral arc, *J. Atmos. Sol. Terr. Phys.*, *72*(7–8), 663–637, doi:10.1016/j.jastp.2010.01.014.
- Davis, T. N. (1978), Observed characteristics of auroral forms, *Space Sci. Rev.*, *22*(1), 77–113, doi:10.1016/j.asr.2003.05.037.
- Donovan, E., et al. (2006), The THEMIS all-sky imaging array – system design and initial results from the prototype imager, *J. Atmos. Sol. Terr. Phys.*, *68*(2006), 1472–1487, doi:10.1016/j.asr.2003.05.037.
- Ebihara, Y. (2007), Aurora Over South Pole Station [online]. Kyoto University: Japan. Available from www.southpole-aurora.org/ [last accessed 2012-09-25].
- Ebihara, Y., Y.-M. Tanaka, S. Takasaki, A. T. Weatherwax, and M. Taguchi (2007), Quasi-stationary auroral patches observed at the South Pole station, *J. Geophys. Res.*, *112*, A01201, doi:10.1029/2006JA012087.
- Ejiri, M., T. Aso, M. Okada, M. Tsutsumi, M. Taguchi, N. Sato, and S. Okano (1999), Japanese research project on Arctic and Antarctic observations of the middle atmosphere, *Adv. Space Res.*, *24*(12), 1689, doi:10.1016/S0273-1177(99)00335-X.
- Fejer, B. G., and M. C. Kelley (1980), Ionospheric irregularities, *Rev. Geophys.*, *18*(2), 401–454, doi:10.1029/RG018i002p00401.
- Frey, H. U., S. Frey, B. S. Lanchester, and M. Kosch (1998), Optical tomography of the aurora and EISCAT, *Ann. Geophys.*, *16*, 1332–1342, doi:10.1007/s00585-998-1332-y.
- Galperin, Y. I. (2001), Multiple scales in auroral plasmas, *J. Atmos. Sol. Terr. Phys.*, *64*(2), 211–229, doi:10.1016/j.asr.2003.05.037.
- Garner, T. W., R. B. Harris, J. A. York, C. S. Herbster, C. F. Minter III, and D. L. Hampton (2011), An auroral scintillation observation using precise, collocated GPS receivers, *Radio Sci.*, *46*, RS1018, doi:10.1029/2010RS004412.
- Gamer, T. W., T. L. Killeen, A. G. Burns, J. D. Winningham, and W. R. Coley (1996), Examination of the oxygen red line signature of a polar cap ionization patch as seen from the Dynamics Explorer 2 satellite, *Radio Sci.*, *31*(3), 607–618, doi:10.1029/96RS00617.
- Hill, T. W. (2004), Auroral structures at Jupiter and Earth, *Adv. Space Res.*, *33*(11), 2021–2029, doi:10.1016/j.asr.2003.05.037.
- Hosokawa, K., J. I. Moen, K. Shiokawa, and Y. Otsuka (2011), Motion of polar cap arcs, *J. Geophys. Res.*, *116*, A01305, doi:10.1029/2010JA015906.
- Kinrade, J., C. N. Mitchell, P. Yin, N. Smith, G. S. Bust, M. J. Jarvis, D. J. Maxfield, M. C. Rose, and A. T. Weatherwax (2011), Ionospheric scintillation over Antarctica during the storm of 5–6 April 2010, *J. Geophys. Res.*, *117*, A05304, doi:10.1029/2011JA017073.
- Kubota, M., H. Fukunishi, and S. Okano (2001), Characteristics of medium- and large-scale TIDs over Japan derived from OI 630-nm nightglow observation, *Earth Planets Space*, *53*(7), 741–751.
- Laundal, K. M., and N. Østgaard (2009), Asymmetric auroral intensities in the Earth's Northern and Southern Hemispheres, *Nature*, *460*(7254), 491–493, doi:10.1038/nature08154.
- Mitchell, C. N., L. Alfonsi, G. De Franceschi, M. Lester, V. Romano, and A. W. Wernik (2005), GPS TEC and scintillation measurements from the polar ionosphere during the October 2003 storm, *Geophys. Res. Lett.*, *32*, L12S03, doi:10.1029/2004GL021644.
- Mitchell, C. N., and P. S. J. Spencer (2003), A three-dimensional time-dependent algorithm for ionosphere imaging using GPS, *Ann. Geophys.*, *46*(4), 687–696.
- Moen, J., S. T. Berry, L. Kersley, and B. Lybekk (1998), Probing discrete auroral arcs by ionospheric tomography, *Ann. Geophys.*, *16*, 574–582, doi:10.1007/s00585-998-0574-z.
- Ngwira, C. M., L. McKinnell, and P. J. Cilliers (2010), GPS phase scintillation observed over a high-latitude Antarctic station during solar minimum, *J. Atmos. Sol. Terr. Phys.*, *72*, 718–725, doi:10.1016/j.jastp.2010.03.014.
- Obara, T., and K. Fukui (1997), Polar auroral arc studies particularly using Akebono satellite and Qaanaaq (Greenland) all-sky imager data, *J. Atmos. Sol. Terr. Phys.*, *59*(96), 1361–1372, doi:10.1016/S1364-6826(96)00187-3.
- Prikryl, P., et al. (2011), Inter-hemispheric comparison of GPS phase scintillation at high latitudes during the magnetic-cloud-induced geomagnetic storm of 5–7 April 2010, *Ann. Geophys.*, *29*, 2287–2304, doi:10.5194/angeo-29-2287-2011.
- Rees, D., M. Conde, Å. Steen, and U. Brändström (2000), The first daytime ground-based optical image of the aurora, *Geophys. Res. Lett.*, *27*(3), 313–316, doi:10.1029/1999GL003696.
- Sandahl, I., U. Brandstrom, and T. Sergienko (2011), Fine structure of aurora, *Int. J. Remote Sens.*, *32*(11), 2947–2972, doi:10.1080/01431161.2010.541507.
- Sandholt, P. E., H. C. Carlson, and A. Egeland (2002), Optical aurora, in *Dayside and Polar Cap Aurora*, Astrophysics and Space Science Library, vol. 270, pp. 33–49, Kluwer, Academic Publishers, Dordrecht, The Netherlands, ISBN:1-4020-0447-8.
- Smith, A. M., C. N. Mitchell, R. J. Watson, R. W. Meggs, P. M. Kintner, K. Kauristie, and F. Honary (2008), GPS scintillation in the high arctic associated with an auroral arc, *Space Weather*, *6*(S03D01), ISSN:1542–7390.
- Strangeways, H. J. (2009), Determining scintillation effects on GPS receivers, *Radio Sci.*, *44*, RS0A36, doi:10.1029/2008RS004076.
- Tanaka, Y.-M., Y. Ebihara, S. Saita, A. Yoshikawa, Y. Obana, and A. T. Weatherwax (2012), Poleward moving auroral arcs observed at the South Pole station and the interpretation by field line resonances, *J. Geophys. Res.*, doi:10.1029/2012JA017899, in press.
- Van Dierendock, A. J. (1999), Eye on the ionosphere: Measuring ionospheric scintillation events from GPS signals, *GPS Solutions*, *2*(4), 60–63.
- Yin, P., et al. (2009), Imaging of the Antarctic ionosphere: Experimental results, *J. Atmos. Sol. Terr. Phys.*, *71*(17-18), 1757–1765, doi:10.1016/j.jastp.2009.09.014.